

3. A. Hubert, R. Schäfer, *Magnetic Domains* (Springer, Berlin, 1998).
4. J. Raabe et al., *J. Appl. Phys.* **88**, 4437 (2000).
5. T. Shinjo, T. Okuno, R. Hassdorf, K. Shigeto, T. Ono, *Science* **289**, 930 (2000).
6. M. Pratzner et al., *Phys. Rev. Lett.* **87**, 127201 (2001).
7. S. Heinze et al., *Science* **288**, 1805 (2000).
8. A. Kubetzka, M. Bode, O. Pietzsch, R. Wiesendanger, *Phys. Rev. Lett.* **88**, 057201 (2002).
9. The Cr film thickness dependent reorientation transition may be caused by the surface anisotropy that dominates at small thickness.
10. M. Bode, M. Getzlaff, R. Wiesendanger, *Phys. Rev. Lett.* **81**, 4256 (1998).
11. O. Pietzsch, A. Kubetzka, M. Bode, R. Wiesendanger, *Phys. Rev. Lett.* **84**, 5212 (2000).
12. D. Wortmann, S. Heinze, Ph. Kurz, G. Bihlmayer, S. Blügel, *Phys. Rev. Lett.* **86**, 4132 (2001).
13. The spin polarizations of the tip and the sample are defined as $P_{s,T}(E) \equiv (n_{s,T}^{\uparrow}(E) - n_{s,T}^{\downarrow}(E)) / (n_{s,T}^{\uparrow}(E) + n_{s,T}^{\downarrow}(E))$ with $n_{s,T}^{\uparrow}(E)$ and $n_{s,T}^{\downarrow}(E)$ being the density of states of majority and minority electrons.
14. O. Pietzsch, A. Kubetzka, D. Haude, M. Bode, R. Wiesendanger, *Rev. Sci. Instr.* **71**, 424 (2000).
15. U. Gradmann, G. Liu, H. J. Elmers, M. Przybylski, *Hyperfine Interactions* **57**, 1845 (1990).
16. The tiny bright spots randomly distributed in both images are caused by adsorbates that appear as dips in the topograph (Fig. 2A) and locally change the value of C in Eq. 1; i.e., the signals are not of magnetic origin.
17. The simulations were performed with the OOMMF program, release 1.2 alpha 2 (<http://math.nist.gov/oommf/>) using a lateral grid with a cell size of 1 nm^2 . The shape as well as the averaged island height of 8 nm was taken into account. Because the height of the Fe islands of about 8 nm is only 2.5 to 3 times larger than $\sqrt{A/K_d}$, the magnetization was assumed to be independent of the z coordinate (3, 18).
18. U. Gradmann, J. Korecki, G. Waller, *Appl. Phys. A* **39**, 101 (1986).
19. The small deviation between experimental and simulated data at $d_{vc} = 10$ to 15 nm in the presence of external fields is caused by the lateral movement of the vortex core (Fig. 4B), which has not been considered in the simulations. At the rim of the Fe island, the magnetization tilts stronger into the direction of H_{ext} than in the island center.
20. Financial support from the BMBF (grant no. 13N7647) and SFB 508 is gratefully acknowledged.

20 June 2002; accepted 4 September 2002

Microfluidic Large-Scale Integration

Todd Thorsen,¹ Sebastian J. Maerkl,¹ Stephen R. Quake^{2*}

We developed high-density microfluidic chips that contain plumbing networks with thousands of micromechanical valves and hundreds of individually addressable chambers. These fluidic devices are analogous to electronic integrated circuits fabricated using large-scale integration. A key component of these networks is the fluidic multiplexor, which is a combinatorial array of binary valve patterns that exponentially increases the processing power of a network by allowing complex fluid manipulations with a minimal number of inputs. We used these integrated microfluidic networks to construct the microfluidic analog of a comparator array and a microfluidic memory storage device whose behavior resembles random-access memory.

In the first part of the 20th century, engineers faced a problem commonly called the “tyranny of numbers”: there is a practical limit to the complexity of macroscopically assembled systems (*1*). Using discrete components such as vacuum tubes, complex circuits quickly became very expensive to build and operate. The ENIAC I, created at the University of Pennsylvania in 1946, consisted of 19,000 vacuum tubes, weighed 30 tons, and used 200 kW of power. The transistor was invented at Bell Laboratories in 1947 and went on to replace the bulky vacuum tubes in circuits, but connectivity remained a problem. Although engineers could in principle design increasingly complex circuits consisting of hundreds of thousands of transistors, each component within the circuit had to be hand-soldered—an expensive, labor-intensive process. Adding more components to the circuit decreased its reliability, as even a single cold solder joint rendered the circuit useless.

In the late 1950s, Kilby and Noyce solved the “tyranny of numbers” problem for electronics by inventing the integrated circuit. By fab-

ricating all of the components out of a single semiconductor—initially germanium, then silicon—Kilby and Noyce created circuits consisting of transistors, capacitors, resistors, and their corresponding interconnects in situ, eliminating the need for manual assembly. By the mid-1970s, improved technology led to the development of large-scale integration (LSI): complex integrated circuits containing hundreds to thousands of individual components.

Microfluidics offers the possibility of solving similar system integration issues for biology and chemistry. However, devices to date have lacked a method for a high degree of integration, other than simple repetition. Microfluidic systems have been shown to have potential in a diverse array of biological applications, including biomolecular separations (*2–4*), enzymatic assays (*5, 6*), the polymerase chain reaction (*6, 7*), and immunohybridization reactions (*8, 9*). These are excellent individual examples of scaled-down processes of laboratory techniques, but they are also stand-alone functionalities, comparable to a single component within an integrated circuit. The current industrial approach to addressing true biological integration has come in the form of enormous robotic fluidic workstations that take up entire laboratories and require considerable expense, space, and labor, reminiscent of the macroscopic approach to circuits consisting of massive vacuum

tube-based arrays in the early 20th century.

There are two basic requirements for a microfluidic LSI technology: monolithic microvalves that are leakproof and scalable, and a method of multiplexed addressing and control of these valves. We previously presented a candidate plumbing technology that allows fabrication of chips with monolithic valves made from the silicone elastomer polydimethylsiloxane (PDMS) (*10*). Here, we describe a microfluidic multiplexing technology and show how it can be used to fabricate silicone devices with thousands of valves and hundreds of individually addressable reaction chambers. As possible applications of fluidic LSI technology, we describe a chip that contains a high-density array of 1000 individually addressable picoliter-scale chambers that serves as a microfluidic memory storage device, and a second chip analogous to an array of 256 comparators.

Our microfluidic multiplexors are combinatorial arrays of binary valve patterns that increase the processing power of a network by allowing complex fluid manipulations with a minimal number of controlled inputs. Although simple microfluidic arrays can be designed in which each fluid channel is controlled by its own individual valve control channel, this non-integrated strategy cannot be efficiently scaled up and thus faces problems similar to those encountered in pre-LSI electronic circuits. In contrast, multiplexors work as a binary tree (Fig. 1) and allow control of n fluid channels with only $2 \log_2 n$ control channels. We fabricated the devices with established multilayer soft lithography techniques (*11*), using two distinct layers. The “control” layer, which harbors all channels required to actuate the valves, is situated on top of the “flow” layer, which contains the network of channels being controlled. All biological assays and fluid manipulations are performed on the flow layer. A valve is created where a control channel crosses a flow channel. The resulting thin membrane in the junction between the two channels can be deflected by hydraulic actuation. Simultaneous addressing of multiple noncontiguous flow channels is accomplished by fabricating control

¹Biochemistry and Molecular Biophysics Option, ²Department of Applied Physics, California Institute of Technology, Pasadena, CA 91125, USA.

*To whom correspondence should be addressed. E-mail: quake@caltech.edu

Direct Observation of Internal Spin Structure of Magnetic Vortex Cores

A. Wachowiak, J. Wiebe, M. Bode,* O. Pietzsch, M. Morgenstern, R. Wiesendanger

Thin film nanoscale elements with a curling magnetic structure (vortex) are a promising candidate for future nonvolatile data storage devices. Their properties are strongly influenced by the spin structure in the vortex core. We have used spin-polarized scanning tunneling microscopy on nanoscale iron islands to probe for the first time the internal spin structure of magnetic vortex cores. Using tips coated with a layer of antiferromagnetic chromium, we obtained images of the curling in-plane magnetization around and of the out-of-plane magnetization inside the core region. The experimental data are compared with micromagnetic simulations. The results confirm theoretical predictions that the size and the shape of the vortex core as well as its magnetic field dependence are governed by only two material parameters, the exchange stiffness and the saturation magnetization that determines the stray field energy.

Detailed understanding of the magnetism of nanostructures is a major requirement for the future progress in magnetic data storage technology. For example, circular nanostructures that exhibit a curling in-plane magnetic configuration (vortex) are considered as basic elements for the magnetoelectronic random access memory (MRAM) (1). The stability and switching behavior of such devices depend on the width of the vortex core, where the magnetization turns into the surface normal. Although detailed theoretical predictions on the width and spin structure of vortex cores are available (2, 3), they have never been proven experimentally.

Recently, magnetic vortex cores were verified by magnetic force microscopy (MFM) (4, 5). However, MFM suffers from three problems: (i) The lateral resolution of MFM typically is limited to ≈ 20 to 100 nm, which is larger than the vortex core. (ii) The magnetic stray field of the tip easily interferes with the vortex as the tip-sample distance becomes too small. (iii) The sensitivity is restricted to the out-of-plane component of the stray field gradient. All three problems are avoided by using spin-polarized scanning tunneling microscopy (SP-STM). First, SP-STM is capable of resolving magnetic domain walls (6) and superstructures down to the atomic scale (7). Second, it has recently been shown that any dipolar interaction between tip and sample can be avoided by the use of antiferromagnetic probe tips (8). Third, by varying the thickness of the antiferromag-

netic layer deposited on the tip, we are able to prepare tips with either in-plane or out-of-plane sensitivity: thick chromium (Cr) films were found to be sensitive to the in-plane component of the sample magnetization, whereas thinner films [thickness < 50 monolayers (ML)] resulted in an out-of-plane sensitivity (9). With this technique we studied the vortex core that appears on iron (Fe) nanoislands, revealing the lateral width of the vortex core, its shape, and its magnetic field dependence.

SP-STM is sensitive to the sample's surface local electron spin density. It makes use of the intrinsic spin polarization of a magnetic tip material serving as a spin filter. It has been shown experimentally (10, 11) and theoretically (12) that topographic and electronic contributions can be successfully separated from the spin signal by means of spectroscopic techniques. The differential conductance measured with spin-polarized scanning tunneling spectroscopy (SP-STs) at the location \vec{r} on the surface for a sample bias voltage U_0 can be written as

$$\frac{dI}{dU}(\vec{r}, U_0)_{sp} = C(1 + P_T P_S \cos\theta) \quad (1)$$

where $C = dI/dU(\vec{r}, U_0)_{SA}$ is the spin-averaged differential conductance, $P_T = P_T(E_F)$ is the spin polarization of the tip at the Fermi energy E_F , and $P_S = P_S(E_F + eU_0)$ is the spin polarization of the sample at the energy $E_F + eU_0$ (13). The angle $\theta = \theta(\vec{M}_T, \vec{M}_S(\vec{r}))$ is enclosed by the tip magnetization \vec{M}_T and the local sample magnetization $\vec{M}_S(\vec{r})$ below the tip apex. On an electronically homogeneous surface, $C(\vec{r})$ and P_S are independent of the location \vec{r} . Therefore, any lateral variation of the dI/dU signal is caused by the $\cos\theta$ term, which—at a fixed

tip magnetization direction—is directly connected to the local orientation of the sample magnetization $\vec{M}_S(\vec{r})$. In the case of antiferromagnetic tips, the magnetic moments cancel out each other and, hence, the net magnetization vanishes but the spin polarization of the outermost tip atom responsible for the tunneling process is preserved. Equation 1 is still valid for antiferromagnetic tips if the term \vec{M}_T is interpreted as the magnetic moment \vec{m} of the atom at the tip apex. Throughout this report, we will continue to use the notation “tip magnetization” \vec{M}_T , though it actually means \vec{m}_T in the case of an antiferromagnetic tip.

The measurements were performed with a low-temperature scanning tunneling microscope (14) at a tip and sample temperature of 14 ± 1 K. A superconducting magnet supplied a magnetic field normal to the surface plane. Nanoscale magnetic particles were prepared under ultra-high vacuum conditions (pressure $p \leq 1 \times 10^{-10}$ mbar) by means of self-organized growth of Fe on the (110) surface of a tungsten (W) single crystal. We evaporated 8 to 10 ML Fe on a stepped W(110) substrate held at room temperature. The sample was thermally annealed for 10 min at 800 ± 100 K, leading to the formation of elongated “islands” with lateral dimensions of 200 to 500 nm by 150 to 250 nm along the [001] and the [110] directions, respectively, and an average height $D = 8$ to 9 nm. The areas between the islands are covered with a single pseudomorphic ML of Fe (15).

The magnetic ground state of Fe islands of that lateral and vertical size is expected to be a vortex. The dimensions of the particles are too large to form a single-domain state because it would cost a relatively high stray field (or dipolar) energy. But they are also too small to form domains like those found in macroscopic pieces of magnetic material because the additional cost of domain wall energy cannot be compensated by the reduction of stray field energy. The magnetization continuously curls around the particle center, drastically reducing the stray field energy and avoiding domain wall energy. For topological reasons, the magnetization in the vortex core has been predicted to turn into the surface normal (Fig. 1).

A constant current topograph of a single Fe island is shown in Fig. 2A. The quasi-hexagonal symmetry of the W(110) surface leads to tapered ends. Step edges of the underlying substrate are weakly visible as a diagonal height modulation caused by the different layer thickness of Fe and W. Though the dI/dU signal on top of such Fe islands is found to be spatially constant if measured with uncovered W tips (not shown), a spatial pattern can be recognized in the dI/dU map (Fig. 2B) measured with a tip

Institute of Applied Physics and Microstructure Research Center, University of Hamburg, Jungiusstr. 11, D-20355 Hamburg, Germany.

*To whom correspondence should be addressed. E-mail: mbode@physnet.uni-hamburg.de

coated with more than 100 ML of Cr. This variation is caused by spin-polarized tunneling between the magnetic sample and the polarized tip. Because this particular tip also showed a strong domain contrast on the pseudomorphic Fe ML (6), the easy axis of which is the $[1\bar{1}0]$ direction, we conclude that \vec{M}_T is parallel to the surface plane and is approximately oriented along the $[1\bar{1}0]$ direction. Four different regions, referred to as domains, can be distinguished in Fig. 2B. Assuming $P_T > 0$ and $P_S > 0$, the observed pattern can be explained by a local sample magnetization $\vec{M}_S(\vec{r})$ that is parallel (bottom) and antiparallel (top) to \vec{M}_T , respectively. An intermediate contrast in the left and the right domain shows that \vec{M}_T and $\vec{M}_S(\vec{r})$ are almost orthogonal ($\cos\theta = 0$). A corresponding domain pattern exhibiting a flux-closure configuration is indicated by the arrows in Fig. 2B. However, because neither the absolute direction of \vec{M}_T nor the sign of P_T and P_S is known, the opposite sense of rotation would also be consistent with the data.

We have zoomed into the central region where the four “domains” touch and where the rotation of the magnetization into the surface normal is expected. Maps of the dI/dU signal measured with Cr-coated tips that are sensitive to the in-plane and out-of-plane component of \vec{M}_S are shown (Fig. 3, A and B, respectively). The dI/dU signal as measured along a circular path at a distance of 19 nm around the vortex core (circle in Fig. 3A) is plotted in Fig. 3C. The cosine-like modulation indicates that the in-plane component of $\vec{M}_S(\vec{r})$ continuously curls around the vortex core. Figure 3B, which was measured with an out-of-plane sensitive tip on an identically prepared sample, exhibits a small bright area approximately in the center of the island. Because \vec{M}_T of this tip is perpendicular to the surface plane, Eq. 1 provides $\cos\theta = 0$ as long as the $\vec{M}_S(\vec{r})$ exhibits no out-of-plane component as in the domain regions. Therefore, the dI/dU map of Fig. 3B confirms that the local magnetization $\vec{M}_S(\vec{r})$ in the vortex core is tilted normal to the surface (Fig. 1) (16). Figure 3D shows dI/dU line sections measured along the lines in (A) and (B) across the vortex core. It was predicted theoretically (2, 3) that the shape of a vortex core is determined by the minimum of the total energy, which is dominated by the exchange and the magnetostatic or demagnetization energy. Compared with the latter, the magneto-crystalline anisotropy energy, which is relevant for the width of bulk Bloch walls, and the surface anisotropy are negligible as long as thin films made of soft magnetic materials like Fe are used. For the thin-film limit (i.e., $D = 0$), it has been shown (2, 3) that the vortex width as defined by the slope of the in-plane magnetization component in the vortex center is

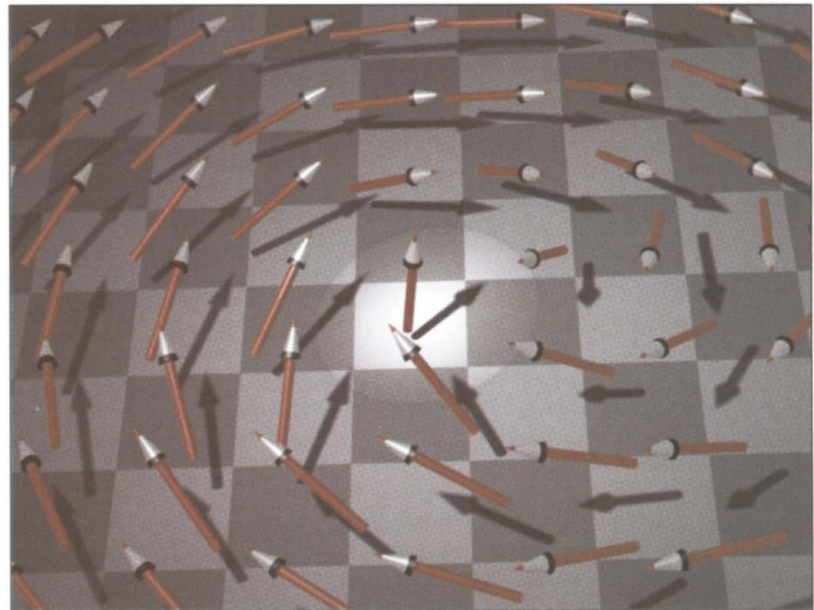
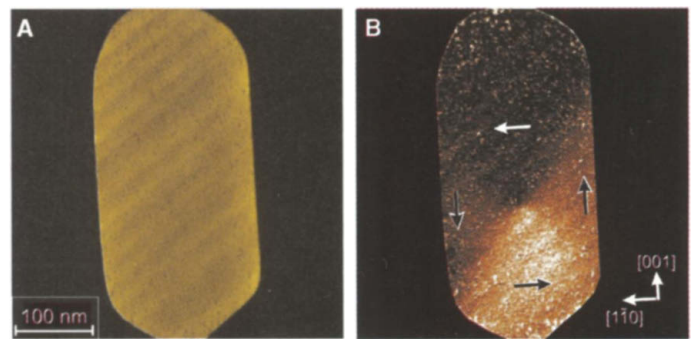


Fig. 1. Schematic of a vortex core. Far away from the vortex core the magnetization continuously curls around the center with the orientation in the surface plane. In the center of the core the magnetization is perpendicular to the plane (highlighted).

Fig. 2. (A) Topography and (B) map of the dI/dU signal of a single 8-nm-high Fe island recorded with a Cr-coated W tip. The vortex domain pattern can be recognized in (B). Arrows illustrate the orientation of the domains. Because the sign of the spin polarization and the magnetization of the tip is unknown, the sense of vortex rotation could also be reversed. The measurement parameters were $I = 0.5$ nA and $U_0 = +100$ mV. The crystallographic orientations were determined by low-energy electron diffraction.



$w_{D=0} = 2\sqrt{A/K_d} \approx 6.4$ nm, where A is the exchange stiffness and $K_d = \mu_0 M_{\text{sat}}^2/2$ is the magnetostatic energy density with M_{sat} as the saturation magnetization. This value is in reasonable agreement with the experimental result $w_{\text{exp}} = 9 \pm 1$ nm. The remaining discrepancy is caused by the finite thickness of the islands ($D \approx 2.5\sqrt{A/K_d}$) in agreement with more elaborate theory (2, 3).

Looking at the shape of the vortex core in more detail, Fig. 4A shows the dI/dU map of an Fe island as measured with a mostly out-of-plane sensitive Cr-coated tip at zero field. Again, the vortex core appears as a bright spot approximately in the center of the island. A radial line profile is shown as a gray line in Fig. 4C. In order to improve the signal-to-noise ratio, the dI/dU signal has been averaged on circles of a radius d_{vc} around the vortex core. Due to the circular symmetry (Fig. 1), this also removes any in-plane contribution

to the measured signal, and only the part of the dI/dU signal that contains information on the perpendicular magnetization M_z remains.

The experimental results are compared with micromagnetic simulations (17) using Fe bulk parameters for A , M_{sat} , and the magneto-crystalline anisotropy K . The resulting normalized perpendicular magnetization M_z/M_{sat} is also shown in Fig. 4C (●). To compensate for the uncertainty in the knowledge of C and $P_S \cdot P_T$ in Eq. 1, we scaled and shifted the experimental data. Thereby, we ensure for a value of 1 in the center of the core and 0 far away from the core as expected for the out-of-plane component. Excellent agreement between the measurement and the simulation is found. Experimental and calculated data are plotted at an enhanced y scale in Fig. 4D. At $d_{\text{vc}} \approx 18$ nm, a weak component in the direction opposite to the central area appears in the calculated data (3, 4). It is also

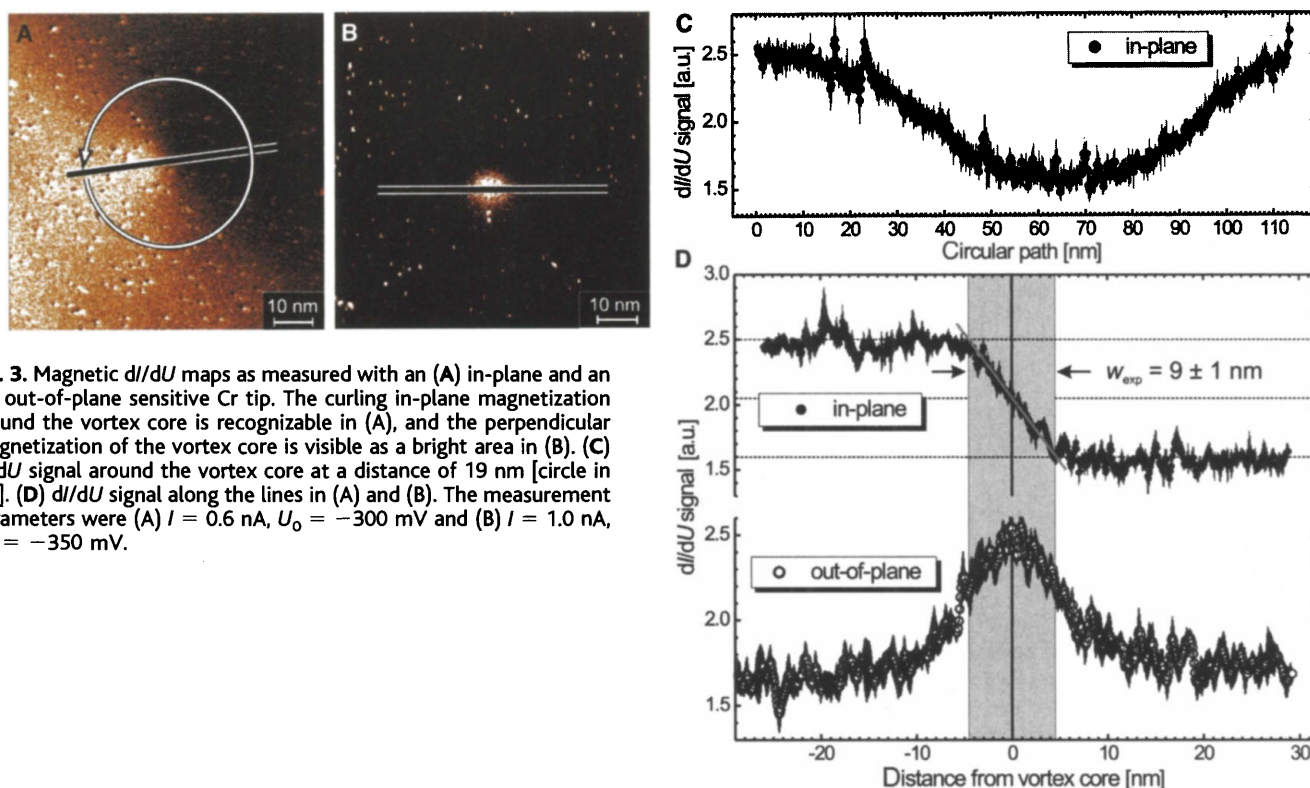
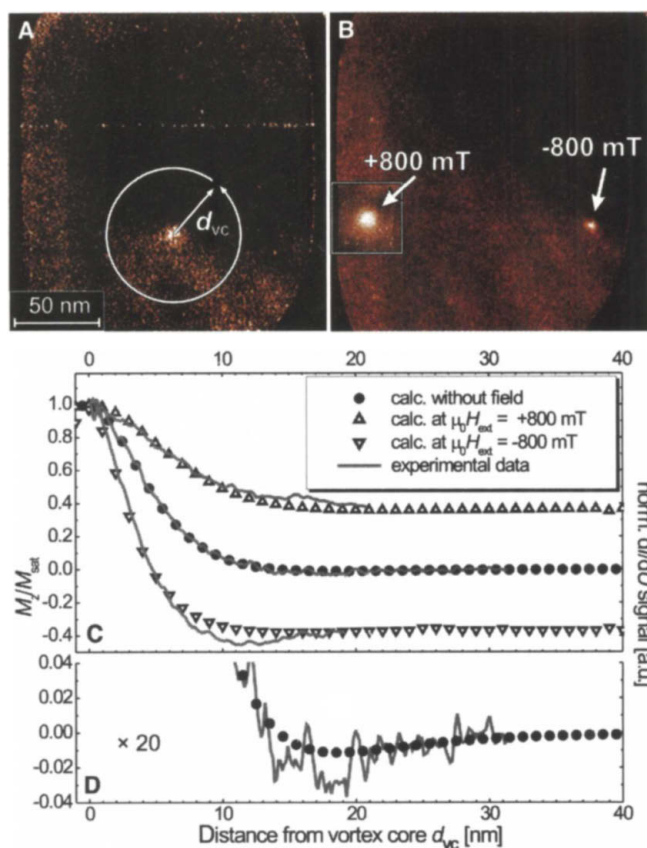


Fig. 3. Magnetic dI/dU maps as measured with an (A) in-plane and an (B) out-of-plane sensitive Cr tip. The curling in-plane magnetization around the vortex core is recognizable in (A), and the perpendicular magnetization of the vortex core is visible as a bright area in (B). (C) dI/dU signal around the vortex core at a distance of 19 nm [circle in (A)]. (D) dI/dU signal along the lines in (A) and (B). The measurement parameters were (A) $I = 0.6$ nA, $U_0 = -300$ mV and (B) $I = 1.0$ nA, $U_0 = -350$ mV.

Fig. 4. dI/dU maps measured with an out-of-plane sensitive Cr tip at (A) zero field and (B) a perpendicular field $\mu_0 H_{\text{ext}} = -800$ mT. The inset shows the vortex core at the position it is found at $\mu_0 H_{\text{ext}} = +800$ mT. The measurement parameters were $I = 0.5$ nA and $U_0 = -0.3$ V. (C) Experimental (lines) and calculated data of the perpendicular magnetization of the vortex core at (●) zero field, (▲) $\mu_0 H_{\text{ext}} = +800$ mT, and (▼) $\mu_0 H_{\text{ext}} = -800$ mT. (D) Magnified representation of the zero field data in (C). At a distance of ≈ 18 nm, both experimental and calculated data show a weak magnetization opposite to the magnetization in the vortex core.



We also investigated the influence of an external field on the vortex core. Figure 4B shows dI/dU maps of the island of Fig. 4A in a perpendicular field of $\mu_0 H_{\text{ext}} = -800$ mT. The vortex core is pushed away from the center of the island, toward its right rim. This lateral movement is caused by a non-perfect alignment of the externally applied field with the island's surface normal (3). The application of a positive field ($\mu_0 H_{\text{ext}} = +800$ mT) causes the vortex core to move in the opposite direction, toward the left rim. More important, averaged radial sections of the experimental dI/dU data reveal that the vortex becomes narrower as the external field is negative; as the field is positive, the vortex becomes broader. Qualitatively, this field-dependence can easily be understood: The energy, which has to be paid for the perpendicular magnetization of the vortex core, increases for an antiparallel and decreases for a parallel orientation to the external field. The micromagnetic simulations reproduce these trends quantitatively (19) and, moreover, show that the magnetization of the whole island, which was in-plane except for the vortex core at zero field, is tilted into the field direction.

References and Notes

1. K. Bussmann, G. A. Prinz, S.-F. Cheng, D. Wang, *Appl. Phys. Lett.* **75**, 2476 (1999).
2. E. Feldtkeller, H. Thomas, *Phys. Kondens. Mater.* **4**, 8 (1965).

found experimentally. As already mentioned (3), this reversed component is caused by partial flux closure of the magnetic stray field of

the vortex core. Although this effect only amounts to 1% of M_{sat} , it is recognizable in the experimental data.